



Cite this: *Phys. Chem. Chem. Phys.*,
2015, 17, 1728

Thermostability and reversibility of silver nanoparticle–protein binding†

Bo Wang,^a Shane A. Seabrook,^b Praveen Nedumpully-Govindan,^a Pengyu Chen,^c Hong Yin,^d Lynne Waddington,^b V. Chandana Epa,^b David A. Winkler,^{de} Jason K. Kirby,^f Feng Ding^{*a} and Pu Chun Ke^{*be}

The interactions between nanoparticles (NPs) and proteins in living systems are a precursor to the formation of a NP–protein “corona” that underlies cellular and organism responses to nanomaterials. However, the thermodynamic properties and reversibility of NP–protein interactions have rarely been examined. Using an automated, high-throughput and temperature-controlled dynamic light scattering (DLS) technique we observed a distinct hysteresis in the hydrodynamic radius of branched polyethyleneimine (BPEI) coated-silver nanoparticles (bAgNPs) exposed to like-charged lysozyme during the processes of heating and cooling, in contrast to the irreversible interactions between bAgNPs and oppositely charged alpha lactalbumin (ALact). Our discrete molecular dynamics (DMD) simulations offered a new molecular insight into the differential structure, dynamics and thermodynamics of bAgNPs binding with the two protein homologs and further revealed the different roles of the capping agents of citrate and BPEI in NP–protein interactions. This study facilitates our understanding of the transformation of nanomaterials in living systems, whose implications range from the field study of nanotoxicology to nanomaterials synthesis, nanobiotechnology and nanomedicine.

Received 30th October 2014,
Accepted 20th November 2014

DOI: 10.1039/c4cp04996a

www.rsc.org/pccp

Introduction

Recently, understanding the biological responses to engineered nanomaterials has become an area of research focus, driven by the crucial need of addressing the transformation, function and safety of nanomaterials introduced into living systems through intentional administration or accidental exposure.^{1,2} Compared with the rapidly growing literature on the electronic, photonic and catalytic applications of nanomaterials, fundamental interactions involving nanoparticles (NPs) and biomolecular species

are less studied and understood, partly due to the myriad and complex nature of such interactions, and partly due to the lack of effective methodologies for capturing atomic- and molecular-level nano-bio interactions.³ Nonetheless, it is generally recognized that understanding fundamental NP–biomolecular interactions is vital to delineating and predicting the cellular and organism responses to NPs, and is essential for enabling the bottom-up design of nanobiotechnology and nanomedicine.⁴

Proteins are a major class of macromolecules that carry out all biological functions *in vivo*. Upon exposure to NPs, the adsorption of proteins, nucleic acids, ions and lipids gives rise to a generic NP–protein “corona”.^{4,5} On one hand, the formation of the NP–protein corona reflects the thermodynamic nature of NP–biomolecular interactions towards a minimized surface energy of the NPs in a biological milieu. On the other hand, the protein corona shields the physicochemical properties of the NPs to elicit their biological identity.⁴ Collectively, the combined NP–protein corona entity is believed to play a central role in determining the transformation, fate and toxicity of NPs in biological systems.

The formation, dynamics and biological identity of the protein corona has been studied intensively in recent years.^{5–13} Specifically, the adsorption of the protein corona has been shown highly dependent on the physicochemical properties of the NPs (size, shape, surface coating, charge, hydrophobicity and chemical composition), the structure of the proteins and the

^a Department of Physics and Astronomy, Clemson University, Clemson, SC, 29634, USA

^b CSIRO Materials Science and Engineering, 343 Royal Parade, Parkville, VIC 3052, Australia. E-mail: fding@clemson.edu, puchun.ke@csiro.au

^c Department of Mechanical Engineering, University of Michigan, Ann Arbor, MI, 28109, USA

^d CSIRO Materials Science and Engineering, Bayview Avenue, Clayton, VIC 3168, Australia

^e Monash Institute of Pharmaceutical Sciences, 390 Royal Parade, Parkville, VIC 3052, Australia

^f CSIRO Land and Water, Waite Road-Gate 4, Glen Osmond, SA 5064, Australia

† Electronic supplementary information (ESI) available: DLS measurements for bAgNP–lysozyme and bAgNP–ALact heated from room temperature to 71.4 °C and cooled back to room temperature. DMD simulations of PEI and citrate binding with AgNP, multiple PEI binding with AgNP, and the folding intermediate of lysozyme. See DOI: 10.1039/c4cp04996a

composition of the biological medium.^{4–6} The residence time of the proteins on the NP surface varies according to the affinities of the protein species for the NPs, as prescribed by the Vroman effect,¹⁴ to give rise to a “soft” or a “hard” corona.⁴ Using discrete molecular dynamics (DMD) simulations, we have recently revealed rapid exchanges between the citrate capping agent of a silver nanoparticle (AgNP) and ubiquitin, especially during the onset of the AgNP-ubiquitin corona formation.¹² By adjusting the surface hydroxylation of a fullerene, we have demonstrated the feasibility of a role reversal in rendering a ubiquitin core confined by the NP.¹⁵ Furthermore, corona-free zwitterionic gold NPs have been synthesized by Moyano *et al.* by tailoring the hydrophobicity of the synthesized NPs, and cell uptake of such covalently functionalized NPs has been shown to depend upon the chemical motifs of the NP surface.¹⁶ With regard to the biological responses to the protein corona, unfolding of fibrinogen by poly(acrylic acid)-conjugated gold NPs promoted Mac-1 receptor activation and inflammation,⁹ while transferrin-functionalized SiO₂ NPs displayed a compromised *in vitro* targeting capability as a result of the corona formation.⁸ Despite these efforts, however, the thermodynamics^{17,18} and reversibility of NP-protein interactions, two important aspects which underlie the transformation, function and toxicity of NPs in biological systems, have been little studied and hence constitute the motivation of the present work.

The two protein species used in this study are hen egg-white lysozyme and bovine milk alpha lactalbumin (ALact). Lysozyme (129 residues, 41% helical and 9% beta sheets) and ALact (120 residues, 41% helical and 9% beta sheets) are viewed as homologs due to their strong resemblance in molecular weight and percentage distribution of secondary structures. However, these two classes of proteins possess entirely opposite net charges. Functionally, lysozyme is responsible for the breakage of peptidoglycans in bacterial cell wall, while the globular metalloprotein of ALact is present in the milk of all mammals serving as a regulator for lactose biosynthesis. Lysozyme and ALact are selected as model proteins in this study because of their biological abundance and contrasting physicochemical properties, including their similarities in molecular weight and globular size, but disparity in sequence and charge.

AgNPs represent a major class of nanomaterials that are produced in large quantities by commercial sources and research laboratories, taking advantage of their antibacterial property^{19,20} and their superb capacity in inducing surface plasmon resonance for biological and chemical sensing and DNA hybridization. The synthesis as well as storage of AgNPs usually involves the use of citrate, polyvinylpyrrolidone (PVP) and, more recently, branched polyethyleneimine (bPEI) polymers,²¹ that are adsorbed onto the NP surface through van der Waals (VDW) and electrostatic forces to render water solubility and steric separations to the NPs. Due to the increasing application of bPEI-coated AgNPs (bAgNPs in short) and paucity of information on the transformation and behavior of bAgNPs within the biological context,²² we examined the thermodynamic interactions between bAgNPs and the protein species of lysozyme and ALact. We further evaluated the effects of these physical interactions on the structural stability of the proteins.

This paper is organized as follows: the surface charges of lysozyme, ALact and bAgNPs are first determined and the formation of the NP-protein coronas is visualized by transmission electron microscopy (TEM). As a central component of the study, the hydrodynamic size and stability of the proteins in the presence of the NPs are characterized using an automated, high-throughput and temperature-controlled dynamic light scattering (DLS) device. To evaluate the biophysical effects of NPs, changes in the secondary structures of lysozyme and ALact upon their interactions with bAgNPs are quantified by circular dichroism (CD) spectroscopy. In addition to the experimental studies, the structural stability of single proteins resulting from their interactions with bAgNPs at elevated temperatures is examined by the state-of-the-art DMD simulations. This study offers a new molecular insight into the little known thermodynamics and reversibility of NP-protein interactions and provides a synergic experimental-computational strategy for facilitating our comprehension of the biological and toxicological implications of engineered nanomaterials.

Results and discussion

Zeta potentials of bAgNPs and proteins

The zeta potentials of the proteins and the NPs in Milli-Q water were determined as +12.1 (± 1.6) mV for lysozyme, -14.6 (± 3.3) mV for ALact and +25.8 (± 1.5) mV for bAgNPs. In comparison, the zeta potentials were +16.5 (± 0.8) mV for the mixture of bAgNP-lysozyme and -13.2 (± 1.1) mV for the mixture of bAgNP-ALact, respectively. The similarity of the zeta potentials of ALact and bAgNP-ALact suggests a comprehensive coating of the negatively charged protein onto the positively charged NPs through electrostatic attraction, a feature not shared by the positively charged lysozyme and bAgNPs due to their mutual repulsion. This observation was further corroborated by the TEM and DLS measurements as well as DMD simulations, as detailed in the following sections.

TEM imaging of NP-protein corona

The TEM imaging showed that the bAgNPs were of ~20 nm in diameter and each NP was coated by a thin bPEI polymer layer of ~1.7 nm (Fig. 1A), in agreement with the manufacturer's specifications. Both the lysozyme and ALact controls appeared globular of 5 nm or less in size (Fig. 1B and C). In comparison, the mixture of bAgNP-lysozyme (Fig. 1D) after 2 h of incubation displayed a size distribution similar to that of bAgNPs alone, implying the lack of corona formation for the like-charged NPs and protein, in agreement with the zeta potential measurement. The mixture of bAgNP-ALact (Fig. 1E and F), in contrast, rendered protein coronas of approximately 3–11 nm in thickness, indicating the strong binding between the oppositely charged species and coating of single- to multi-layer proteins on the NP surfaces.

Hydrodynamic size of bAgNP-protein

As shown in Fig. 2A, the hydrodynamic radius of lysozyme remained at ~2.1 nm (± 0.3 nm of standard deviation) for the entire temperature range of 18–53.4 °C. This is understandable

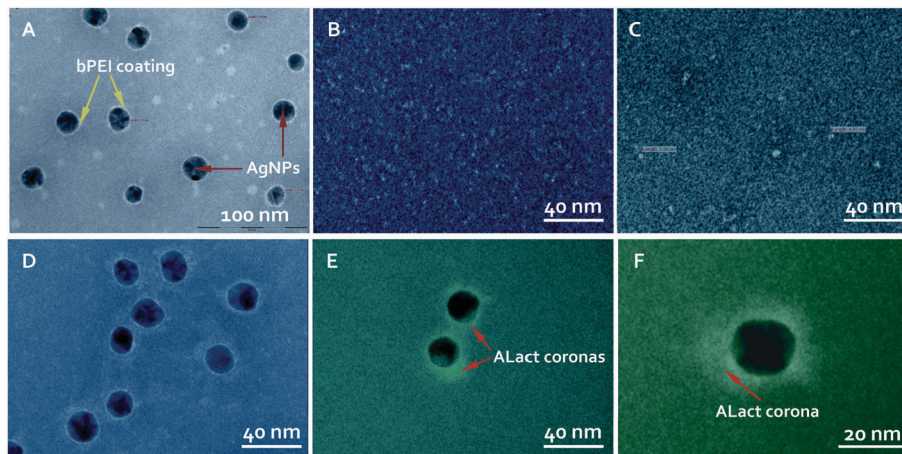


Fig. 1 TEM images of bAgNPs (A), lysozyme (B), ALact (C), bAgNP–lysozyme (D), and bAgNP–ALact (E, F). The thin white layer of ~1.7 nm surrounding each bAgNP (yellow arrows) is presumably the bPEI polymer coating (A, D). Both lysozyme and ALact appear as small white globules of 5 nm or less. The arrows in (E) and (F) indicate ALact coronas of ~3–11 nm in thickness on the bAgNP surfaces.

considering that melting of lysozyme occurs at ~73 °C.¹⁸ The hydrodynamic radius of bAgNPs was 14.7 (± 0.2) nm throughout the same temperature range (Fig. 2B), indicating the thermal stability of the polymer-coated NPs. In contrast, when bAgNPs and lysozyme were mixed at respective concentrations of 0.088 mg mL⁻¹ and 0.9 mg mL⁻¹, to ensure an abundance of the protein for a hypothetical NP–protein corona based on a geometrical estimation,¹⁸ heating from room temperature to 53.4 °C induced an increase from 14.7 (± 0.5) nm to 16.7 (± 0.2) nm in the hydrodynamic radius of the mixture, while cooling caused a reversed process characterized by a distinct hysteresis (Fig. 2C and D). The 13.6% increase in the hydrodynamic radius over elevated temperatures suggests a swelling induce by thermal agitation in the radius of gyration (R_g) of lysozyme. The hysteresis points to a reversible process of bAgNP–lysozyme interactions, probably resulting from the electrostatic repulsion between the like-charged NPs and the protein. Consistently, the histograms of the bAgNP–lysozyme hydrodynamic radius in Fig. 2E and F display a strong resemblance, with the cooling process inducing a slightly broader but still similar distribution compared with the heating process. Since the hydrodynamic radius of the bAgNP–lysozyme mixture mirrors that of the bAgNPs alone, and in consideration of the principle of DLS that the intensity of light scattering is proportional to the sixth power of the particle diameter, we infer that there was no substantial formation of a NP–protein corona for the mixture of bAgNP–lysozyme. This prognosis is consistent with the TEM observations (Fig. 1D).

In contrast to the bAgNP–lysozyme interactions, the binding between bAgNPs and ALact induced marked increases in the hydrodynamic radius of the bAgNP–ALact mixture. As shown in Fig. 3A and B the hydrodynamic radius of the ALact control increased from 2.1 (± 0.2) nm to 6.4 (± 2.2) nm during heating from room temperature to 53.4 °C and scaled back to 3.3 (± 0.7) nm during cooling, suggesting the role of thermal agitation in compromising the structural stability of ALact. In comparison, the hydrodynamic radius of the bAgNP–ALact mixture rose rapidly to 54 nm at room temperature and increased further

to as high as 247.7 nm at 53.4 °C, further characterized by a pronounced broad distribution (± 144.1 nm at 53.4 °C, Fig. 3C) to indicate cross linking between the bAgNPs through ALact. Upon cooling, the hydrodynamic radius of the mixture decreased back to 113.9 (± 19.7) nm at room temperature, which is still significantly larger than the value of 53.6 nm prior to heating. Compared with the small hydrodynamic radius of the protein (Fig. 3A and B) and the intermediate size of the NPs (Fig. 2B), and in connection with the TEM imaging (Fig. 1E and F), such large hydrodynamic radii reflect the formation of NP–protein coronas (indicated by the multiple peaks in Fig. 3E) and NP–protein aggregation mediated by electrostatic attraction, hydrophobic interaction and hydrogen bonding between NP–protein and protein–protein. Unlike the bAgNP–lysozyme interactions (Fig. 2C), no clear and repeatable hysteresis was observed for the hydrodynamic radius of bAgNP–ALact through heating and cooling (Fig. 3C and D). Since the hydrodynamic size distributions expand up to three orders of magnitude in the histograms of Fig. 3E and F that are dissimilar in either peak positions or relative intensities, also since there is a lack of prominent peaks around the hydrodynamic radius of bAgNPs (Fig. 3E), we infer that the binding between AgNPs and ALact was strong and irreversible. In addition, formation of NP–protein aggregation appeared more pronounced with increased NP concentrations, as evidenced by a comparison of Fig. 3G and H, where the slope of hydrodynamic radius/temperature was elevated from 8.7 nm °C⁻¹ to 14.3 nm °C⁻¹ when the NP concentration was increased from 0.044 mg mL⁻¹ to 0.154 mg mL⁻¹, with the protein concentration fixed at 0.9 mg mL⁻¹.

Although both bAgNPs and lysozyme remained stable up to 71.4 °C (Fig. 2B and Fig. S1A in ESI[†]), the interactions between bAgNPs and lysozyme prompted their mutual aggregation at or above 70 °C, as shown by the sharp departure of the NP–protein hydrodynamic radius from those at lower temperatures in Fig. S1B and S1C (ESI[†]). This phenomenon differs from that in Fig. 2, where heating and cooling of bAgNP–lysozyme was confined between room temperature and an upper limit of 53.4 °C. This implies that the presence of bAgNPs triggered an earlier onset of lysozyme melting,

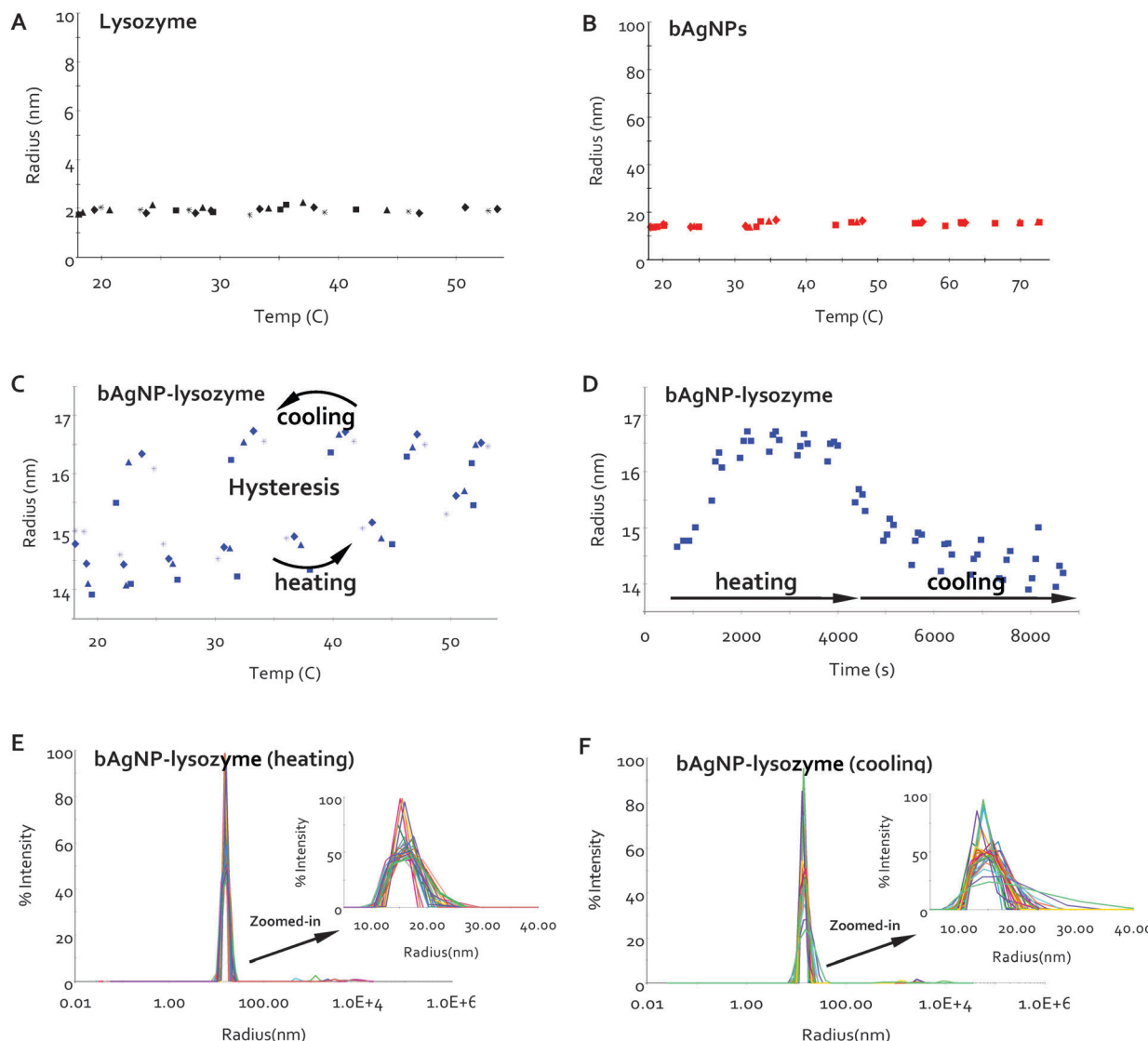


Fig. 2 DLS measurement of bAgNP–lysozyme heated to 53.4 °C (except for (B), where heating extends to 71.4 °C) and cooled back to room temperature. (A) Hydrodynamic radius of the lysozyme control. (B) Hydrodynamic radius of the bAgNP control. (C) Hydrodynamic radius of bAgNP–lysozyme versus temperature, displaying a hysteresis between heating and cooling. (D) Corresponding to (C), hydrodynamic radius of bAgNP–lysozyme versus time. (E, F) Histograms of bAgNP–lysozyme hydrodynamic radius during heating and cooling, with their zoomed-in views shown in insets for more detail. (A–F) Lysozyme: 0.9 mg mL⁻¹ and (B–F) bAgNPs: 0.088 mg mL⁻¹, all in PBS. The diamond, triangles, squares and stars represent data points obtained from different sample wells of the same conditions.

which consequently induced protein–protein and NP–protein aggregations. Notably, cooling from 71.4 °C down to room temperature did not recover the original hydrodynamic radius of 14.7 (± 0.2) nm as assumed by the NP–protein mixture at low temperatures (Fig. S1D vs. Fig. S1B and S1C, ESI†), indicating the irreversible process of bAgNP–lysozyme interactions once the protein had undergone melting and aggregation. Comparatively, the binding of bAgNPs and ALact appeared irreversible for heating and cooling up to 71.4 °C (Fig. S2, ESI†), characteristically similar to that observed for heating and cooling of bAgNP–ALact up to 53.4 °C (Fig. 3).

Changes in protein secondary structure induced by bAgNPs

A CD experiment was performed to provide an insight into the effects of bAgNPs on the secondary structure of the proteins.

As shown in Fig. 4 (raw data see Fig. S3, ESI†), the presence of bAgNPs caused a reduction in the beta sheet component but minimal changes overall in the secondary structure of lysozyme. In comparison, binding with bAgNPs yielded a 20% reduction in the alpha helical content coupled with a 36% increase in the turns of ALact, indicating a stronger impact on the structure of ALact than lysozyme when exposed to bAgNPs, consistent with the TEM and DLS observations.

DMD simulations of bAgNP–protein binding

We performed DMD simulations to examine the binding of a bAgNP with the two types of proteins *in silico*. The AgNP was modeled by a (111) silver surface with ten atom layers. The major physical interactions considered include VDW, solvation energy,

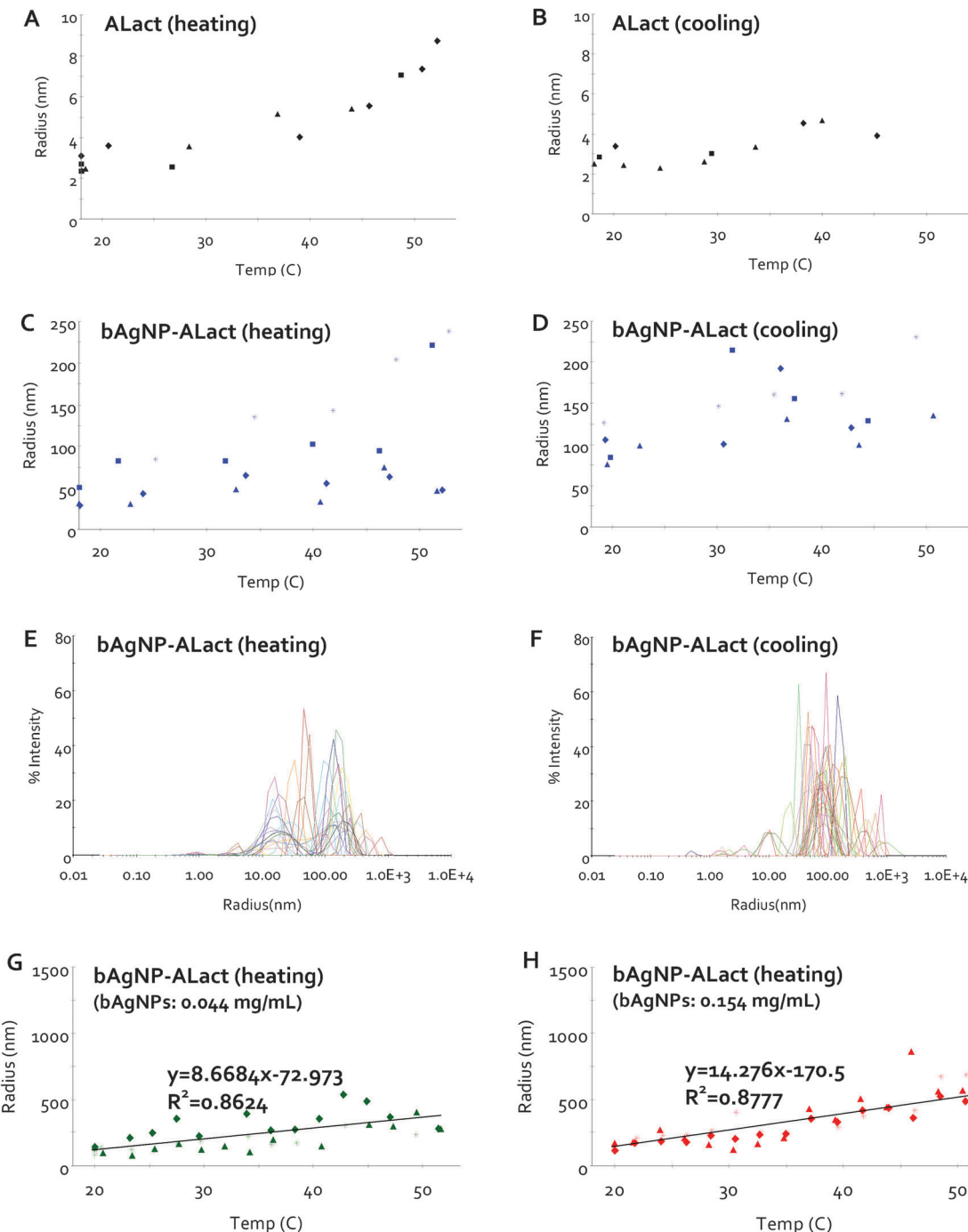


Fig. 3 DLS measurement of bAgNP-ALact heated to 53.4 °C and cooled back to room temperature. (A, B) Hydrodynamic radius of ALact during heating and cooling. (C, D) Hydrodynamic radius of bAgNP-ALact during heating and cooling. (E, F) Histograms of bAgNP-ALact hydrodynamic radius during heating and cooling. (G, H) Hydrodynamic radius of bAgNP-ALact during heating for different NP : protein ratios. The slopes of the fitted linear trendlines are 8.7 and 14.3 nm °C⁻¹, respectively. ALact: 0.9 mg mL⁻¹ (A–H). bAgNPs: 0.088 (B–F), 0.044 (G) and 0.154 mg mL⁻¹ (H). All samples in PBS. The diamond, triangles, squares and stars represent data points obtained from different sample wells.

and the electrostatic interaction of “image” charges. The interaction parameters were adopted from a recently developed AgP molecular mechanics force field²³ (Methods). We first modeled the binding of capping molecules to the NP surface. We used the generation-3 PEI dendrimer to model the bPEI molecule. As a reference, we also studied citrate coating of the NP by DMD simulations. We found

that both PEI and citrate bound to the AgNP surface (Fig. S4B and S4C, ESI†) via charge-“image” charge interactions. In addition, PEI showed a stronger binding to the AgNP than citrate, as reflected by the higher dissociation temperature of the PEI (Fig. S4A, ESI†). This stronger binding of PEI and AgNP was due to the large number of charged amine groups of the polymer. This result is consistent with

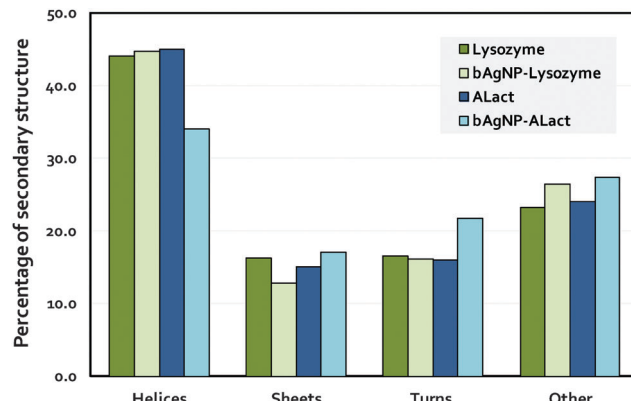


Fig. 4 Changes in the secondary structures of lysozyme and ALact upon binding with bAgNPs. The proteins ($10 \mu\text{g mL}^{-1}$ or $0.7 \mu\text{M}$ in PBS) were pre-incubated with the bAgNPs ($2 \mu\text{g mL}^{-1}$ in PBS) for 2 h at room temperature. The percentages of the secondary structures were calculated by the CDSSTR and CONTIN/LL algorithms of the CDPro package, using SMP56 and SP43 protein reference datasets.

the visual observation that citrate-capped AgNPs displayed a slightly higher propensity for aggregation than bPEI-capped AgNPs. We also performed DMD simulations of multiple PEI binding with an AgNP. Due to the high number of charges of PEI molecules bound to the NP surface, the local salt concentration near the surface was higher than that of the bulk, and consequently, the screening effect near the NP surface was stronger than the bulk. Indeed, in DMD simulations the counter-ions (Cl^-) added to neutralize the system were able to account for the increased screening of the electrostatic repulsion between the highly charged PEI molecules and the strong PEI–AgNP binding allowed a high density of PEI molecules covering the NP surface (Fig. S5, ESI[†]). For example, eight generation-3 PEI molecules were able to cover a surface area of $\sim 8 \times 8 \text{ nm}^2$ with the surface distances between adjacent PEI molecules within or equal to the bulk Debye length, $\sim 1 \text{ nm}$.

Prior to the study of bAgNP–protein binding, we simulated lysozyme and ALact alone in order to evaluate their corresponding folding thermodynamics. We applied the replica exchange DMD simulation method for efficient conformational sampling.^{24,25} Using the weight histogram analysis methods, we computed the specific heat as a function of temperature for both types of proteins (Fig. 5A). Different from ALact, the specific heat plot of lysozyme displays more than one peak within the temperature range of 300 K to 370 K, indicating the population of folding intermediates. The observation of lysozyme folding intermediates has been reported previously.^{26,27} Examination of our simulations indicated that the folding intermediates of lysozyme corresponded to the partial unfolding of the beta-sheet in the native structure (Fig. S6, ESI[†]), which is consistent with the unfolding pathway identified with all-atom MD simulations.²⁸ The high temperature peak in the lysozyme specific heat, T_m , corresponds to the global unfolding where the protein loses its helical content (Fig. 5B). Therefore, lysozyme has a higher melting temperature and better thermostability than ALact, consistent with the experimental observations (Fig. 2A vs. 3A).

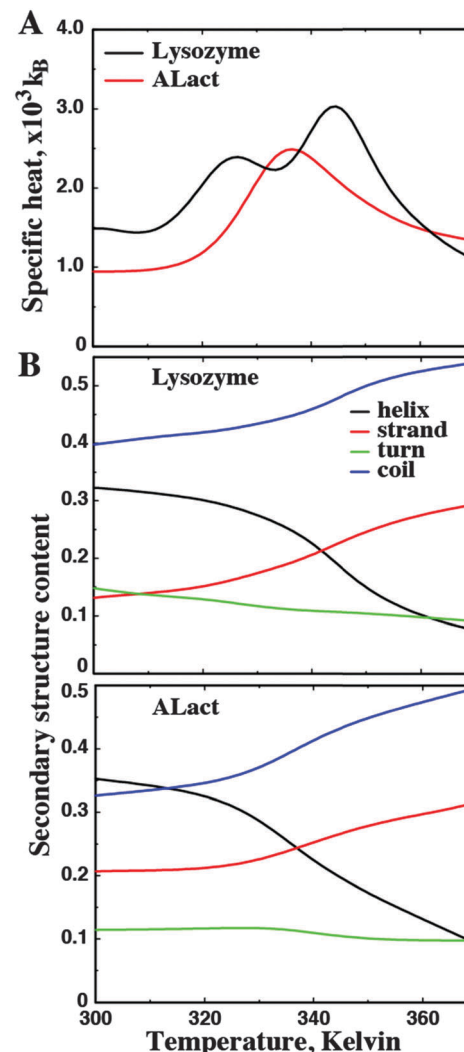


Fig. 5 The folding thermodynamics of lysozyme and ALact derived from DMD simulations. (A) The specific heat as a function of temperature. (B) The secondary structure content of alpha helices, beta strands, turns and coils as functions of temperature.

Next, we performed DMD simulations of protein binding with an AgNP surface covered by multiple PEI molecules (Fig. 6). For each type of the protein species, we performed binding simulations at a wide range of temperatures from 260 K to 360 K. To ensure sufficient sampling at each temperature, we performed multiple independent DMD simulations ($\times 20$) with different initial configurations, including both relative distances and orientations. In all simulations, PEI molecules stayed bound to the AgNP surface. We then calculated the number of intermolecular atomic contacts between a protein and the PEI-capped AgNP, $N_{\text{C}_{\text{protein-NP}}}$. The histogram of intermolecular contacts between lysozyme and bAgNP had only one peak near zero (Fig. 6A), while the same histogram of ALact displayed an additional peak with a large number of inter-molecular contacts (Fig. 6B). The binding with a small number of inter-molecular contacts corresponds to diffusive non-specific interactions that are transient (Fig. 6C). In the case ALact, once the strong binding

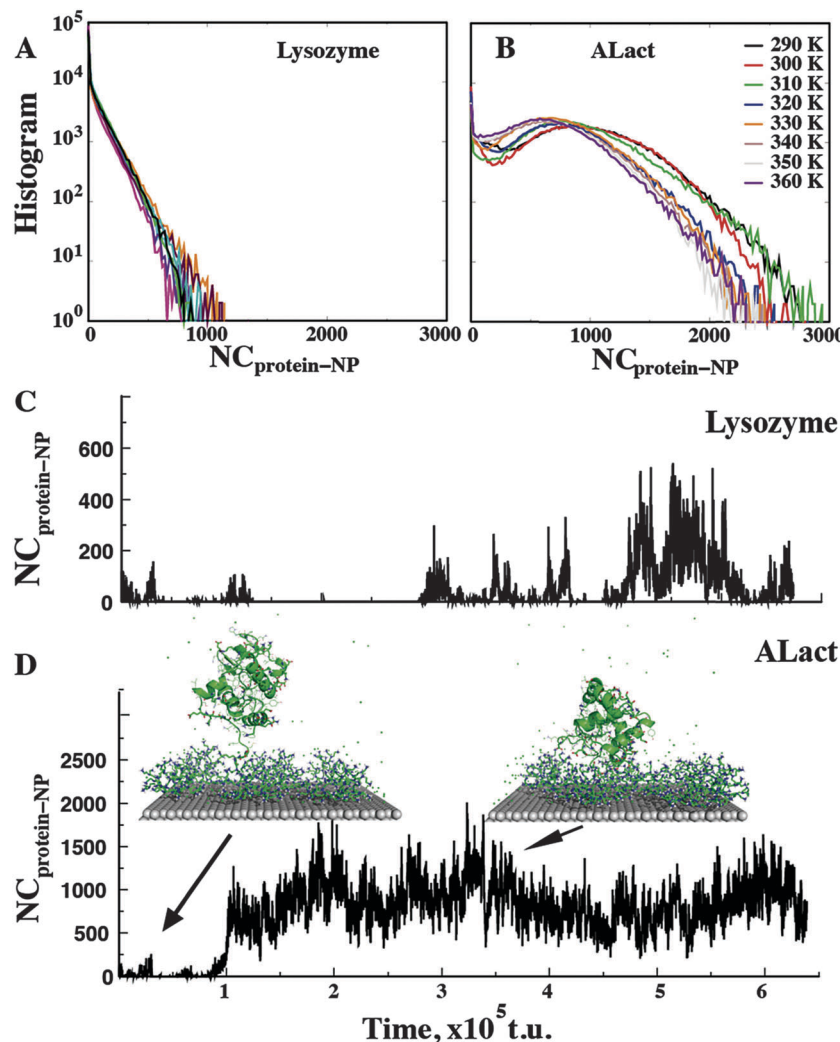


Fig. 6 The binding between a bAgNP and lysozyme (A, C) and ALact (B, D). The histograms of inter-molecular atomic contacts between protein and NP, $NC_{protein-NP}$ for lysozyme (A) and ALact (B) are derived from DMD simulations. Results from different temperatures are included. (C) A representative trajectory of lysozyme and bAgNP binding at $T = 300$ K indicates that the binding is transient and weak. (D) A trajectory of intermolecular contacts between ALact and bAgNP at $T = 300$ K demonstrates both the weak and strong binding modes. The strong binding with an extensive number of inter-molecular contacts is long lasting.

took place the protein stayed bound to the NP during the entire course of the simulations (e.g. Fig. 6D). Therefore, lysozyme showed only weak and transient binding to the bAgNPs, while ALact bound to the positively-charged bAgNPs with a high affinity.

To evaluate the driving force in protein binding, we computed the average number of inter-molecular contacts of protein binding with the AgNP and PEI separately (Fig. 7A and B). We found that the binding was dominated by the interaction between the protein and PEI molecules for both lysozyme and ALact. Due to the electrostatic repulsion between PEIs ($+32e$) and lysozyme ($+7e$), lysozyme binding with bAgNP was weak. Similarly, the strong ALact–bAgNP binding was dominated by the electrostatic attraction between PEI and ALact ($-7e$). Interestingly, in the case of ALact, we did not observe competitions among the capping PEIs for the NP surface, unlike our previous observation of ubiquitin binding with a citrate-capped AgNP.¹² This discrepancy is consistent with the difference in NP-binding

affinities between citrate and PEI (Fig. S4A, ESI†). As the temperature increased within the sampled range, we did not observe any changes in the NP-binding probability of ALact (Fig. 7B). The increasing thermo-fluctuations only reduced the average number of inter-molecular contacts. Therefore, the ALact corona remained stably bound to the AgNP at elevated temperatures.

To evaluate the conformational changes of the proteins due to their binding to a bAgNP, we computed the protein secondary structure contents with and without the bAgNP in DMD simulations (Table 1). We found no significant impact on the lysozyme secondary structure due to its weak binding with the bAgNP. In comparison, binding with the bAgNP exerted a strong effect on ALact, where the alpha-helix and beta-strand contents decreased while the coil content increased. The computational results of changes in protein secondary structures upon bAgNP binding are qualitatively consistent with the CD experiment (Fig. 4), although the exact numbers are not directly comparable due to

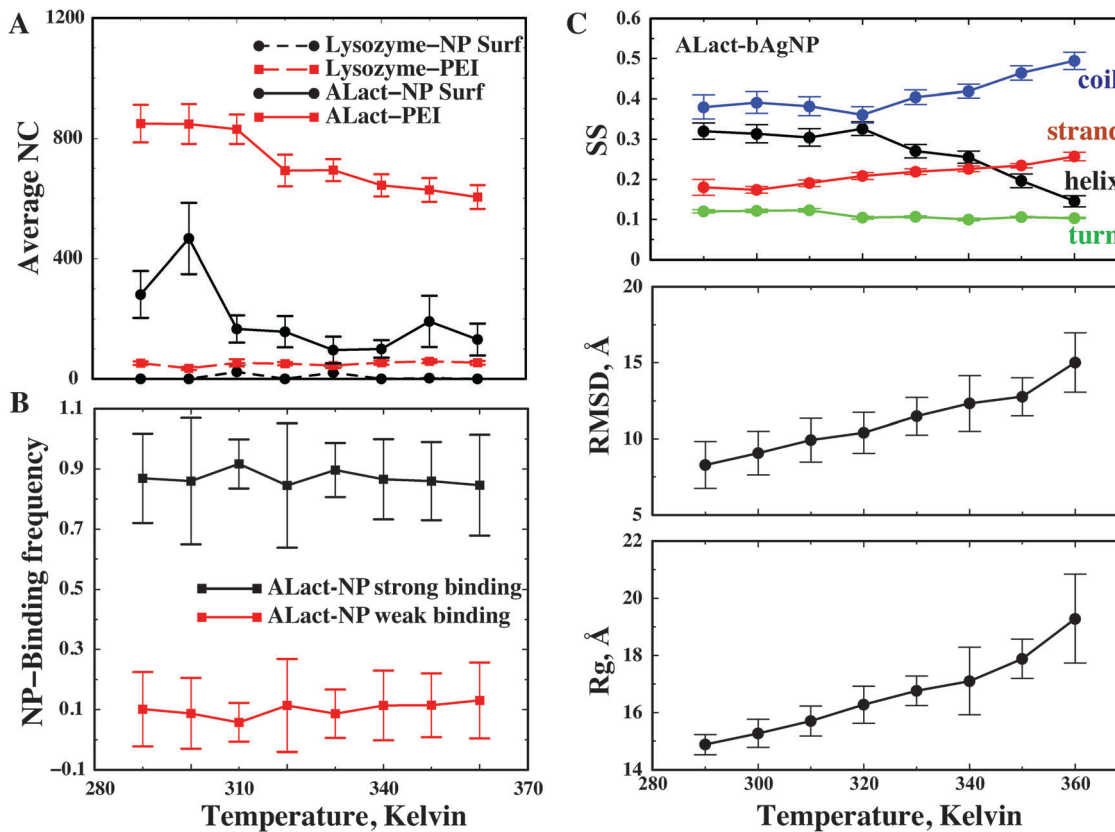


Fig. 7 The thermodynamics of bAgNP binding with proteins. (A) The binding of the proteins with the AgNP surface and with PEI was calculated separately as the function of temperature. (B) The frequency of binding between ALact and bAgNP was computed as the function of temperature. The weak and strong binding was identified separately. (C) The structural properties of ALact bound to bAgNP, including secondary structure contents (SS), root-mean-square deviation (RMSD), and R_g , were computed as the function of temperature. The error bars correspond to standard deviations computed from independent simulations at each temperature.

Table 1 The secondary structure contents of ALact at $T = 300$ K. The results without (w/o) NP binding are obtained from the replica exchange simulations. The results with NP are derived from multiple independent DMD simulations

	Lysozyme		ALact	
	w/o NP	With NP	w/o NP	With NP
Helix	0.34 ± 0.01	0.34 ± 0.01	0.35 ± 0.01	0.31 ± 0.03
Strand	0.17 ± 0.01	0.16 ± 0.01	0.21 ± 0.01	0.17 ± 0.01
Turn	0.13 ± 0.01	0.14 ± 0.01	0.11 ± 0.01	0.12 ± 0.01
Coil	0.36 ± 0.01	0.36 ± 0.01	0.33 ± 0.01	0.40 ± 0.03

the different sample conditions in the two cases. We also calculated other structural parameters of the bAgNP-bound ALact, including the secondary structure contents, root-mean-square deviation (RMSD) and R_g as functions of temperature (Fig. 7C). As temperature increased, the NP-bound protein lost their compact secondary structures like the helices and turns, while the amount of extended conformations of stands and coils increased. The proteins also significantly lost their tertiary structures with increased RMSD and R_g , consistent with the observed increases in the hydrodynamic radius of bAgNP-ALact corona upon heating (Fig. 3C). Due to the well-known challenges in computational modeling of protein refolding, we did not perform the refolding simulations.

However, our computational study suggests that the strong binding of ALact with bAgNPs may trap the protein in the unfolded states, resulting in the experimentally observed irreversibility of binding.

Conclusions

This study has examined the thermodynamics and reversibility of NP-protein interactions, two important aspects which underpin the transformation, function and toxicity of NPs in living systems. Specifically, our combined experimental and computational approach demonstrated that lysozyme and ALact, two homologous proteins with similar structures but distinct sequences and net charges, displayed drastically different binding affinities for bAgNPs (Fig. 2, 3, 6 and 7). The negatively charged ALact ($-7e$) exhibited a strong and irreversible binding to bAgNPs, while the positively charged lysozyme ($+7e$) showed only a weak and transient binding characterized by a distinct hysteresis, as reflected by the contrasting trends in the hydrodynamic radius (Fig. 2 and 3) and average number of contacts of the NP-protein mixtures (Fig. 6 and 7).

Both the CD measurement and DMD simulations (Fig. 4 and Table 1) revealed that binding to bAgNPs had a minimal impact on the secondary structure of lysozyme but a strong effect on

the secondary structure of ALact. When compared with free ALact molecules, binding to AgNPs induced significant losses in its secondary structure. As temperature increased, ALact did not dissociate from the AgNP (Fig. 7B) while kept losing its structures (Fig. 7C), contributing to the increased hydrodynamics radius of the NP–protein corona as observed in the DLS experiment (Fig. 3C). The increase of the ALact hydrodynamics radius could also be induced by the protein-mediated corona–corona binding. Taken together, protein denaturation in a corona and inter-corona protein association resulted in the observed irreversibility of bAgNP–ALact binding upon cooling.

In addition, due to the charge–“image” charge electrostatic attractions, the AgNP surface can bind either positively or negatively charged molecules (Fig. S4, ESI[†]), so that both bPEI and citrate can be used as the capping agents. Our DMD simulations revealed that PEI molecules with a high number of cationic primary amines bound to AgNP stronger than citrate. PEI molecules did not dissociate from the AgNP within a wide range of temperatures while citrates already dissociated (Fig. S4A, ESI[†]). Such strong binding allowed a high capping density of PEIs on the AgNP surface, efficiently stabilizing the AgNP from agglomeration (Fig. S5, ESI[†]). With a high number of PEI molecules covering the AgNP surface that did not dissociate, protein binding with the AgNP was determined by the physicochemical properties of the PEI capping agent, allowing the oppositely charged ALact to bind to the AgNP favorably. This observation differs from the case of protein binding with a citrate-capped AgNP,¹² where weakly-bound citrates were rapidly replaced by ubiquitin molecules upon competitive binding to the AgNP. Therefore, both the surface chemistry and dynamic properties of ligands play an important role in protein binding and, thus, the corona formation. This new insight may prove valuable for guiding nanomaterials design and synthesis.

Methodologically, we were able to develop an all-atom DMD model for AgNP based on the recently published AgP molecular mechanics force field. Due to limitations in computational sampling efficiency, molecular dynamics simulations with silver and gold particles^{23,29,30} have been mostly focused on NP-binding with small organic ligands, amino acids and peptides. The efficient sampling of DMD allowed us to study the structure, dynamics and thermodynamics of the large systems of AgNP–proteins in the presence of capping agents. The recapitulation of various experiments, including differential NP-ligand binding (citrates vs. PEI), bAgNP–protein binding (lysozyme vs. ALact) and changes in protein secondary structure upon bAgNP binding, highlights the predictive power of the DMD approach in studying the nano-bio interface for advancing the fields of nanotoxicology, nanobiotechnology and nanomedicine.

Experimental and computational methods

Sample preparations

BioPure bAgNPs of 20 nm in nominal diameter (0.67 mg mL^{-1} , in water) were purchased from NanoComposix. The stock NP suspension appeared homogeneous and free from precipitation

when stored at 4 °C or diluted in phosphate buffered saline (PBS, pH 7.4) at room temperature. Hen-egg white lysozyme (MW 14 307 Da; isoelectric point 11.35) and bovine milk ALact (MW 14 178 Da; isoelectric point 4.5) were purchased in lyophilized powder form from Sigma-Aldrich. The proteins were then dissolved in PBS to stock solutions of 3 mg mL^{-1} , or $210 \mu\text{M}$, prior to use.

Zeta potential

The zeta potentials of lysozyme, ALact, bAgNPs, and NP–protein mixtures were determined using a DLS device (Zetasizer Nano S90, Malvern Instruments) at room temperature. For this measurement the NP and protein stocks were first diluted in Milli-Q water to 0.5 mg mL^{-1} for the bAgNPs and 0.11 mg mL^{-1} for the proteins. The use of Milli-Q water excluded the complications introduced by the ions in buffer. The NP–protein mixtures were obtained by mixing bAgNPs with lysozyme or ALact at a 1 : 1 volume ratio followed by a 2 h incubation, which ensured a complete coating of the NPs by the proteins based on geometrical estimations.

TEM

The sample solutions/suspensions for TEM imaging were prepared as predescribed for the zeta potential measurement. Conventional TEM does not result in clear visualization of polymers or proteins, as such soft matter are subject to shrinkage or severe radiation damage under the electron beam. Negative staining is a technique commonly used for the imaging of biological specimens, and has been applied here to image both the polymer coating and the protein coronas of bAgNPs.

Carbon-coated 300-mesh copper grids were glow-discharged in nitrogen to render the carbon film hydrophilic. A $4 \mu\text{L}$ aliquot of each sample was pipetted onto a grid. After 30 s of adsorption excess samples were drawn off using Whatman 541 filter paper, followed by staining with $10 \mu\text{L}$ 2% aqueous potassium phototungstate at pH 7.2, for 10 s. Excess stains were drawn off as described before and the grids were air-dried until needed. The samples were examined using a Tecnai 12 Transmission Electron Microscope (FEI, Eindhoven, The Netherlands) at an operating voltage of 120 kV. Images were recorded using a Megaview III CCD camera and AnalySIS camera control software (Olympus). Under TEM the polymer coating and protein coronas appeared as a bright region around the dark central AgNPs, as the regions occupied by the organic material excluded the electron-dense stain, which otherwise appeared as a uniform background of intermediate electron density.

Temperature-controlled DLS

The hydrodynamic sizes *versus* temperature were acquired for lysozyme, ALact, bAgNPs, and NP–protein mixtures using an automated, high-throughput, temperature-controlled DLS device (DynaPro Plate Reader, Wyatt) and black 384-well plates (Thermo Fisher). Prior to mixing, the NP and the protein concentrations were prepared at 0.22 mg mL^{-1} and 3 mg mL^{-1} respectively in PBS. For each NP–protein mixture, the volume of the proteins was fixed at $6 \mu\text{L}$ while the volume of the bAgNPs was varied

from 4 μL to 8 μL and 14 μL . The selection of these concentrations ensured good scattering signals for the DLS device. For the controls the volume of the bAgNPs was 8 μL while that of the proteins was 6 μL , respectively. The total volume of each sample well was topped up to 20 μL by adding PBS. Prior to the DLS measurements the samples were incubated for 2 h and spun for 1 min at 1000 rpm/164 RCF (Centrifuge 5804, Eppendorf) to ensure good mixing. Each sample well was then topped with glycerol of 10 μL to prevent volume loss and concentration variations through heating. The thermal cycler of the DLS device was programmed to an increment rate of 0.52 $^{\circ}\text{C min}^{-1}$ during heating from room temperature to 50 $^{\circ}\text{C}$ (actual temperature recorded: 53.4 $^{\circ}\text{C}$) or 70 $^{\circ}\text{C}$ (actual temperature recorded: 71.4 $^{\circ}\text{C}$), respectively, followed by a decrement rate of 0.52 $^{\circ}\text{C min}^{-1}$ back to room temperature. The selection of 50 $^{\circ}\text{C}$ as one upper limit for heating ensured a temperature range relevant to biological systems, while the selection of 70 $^{\circ}\text{C}$ exploited the full temperature range when lysozyme is not yet denatured. At the end of each heating or cooling step of 5 s, the optical module collected data, which was automatically processed and displayed using the Dynamics 7.1.7 software. To ensure repeatability and statistics each sample condition was measured with triplicates or quadruplicates.

Circular dichroism spectroscopy

To access the effects of NP binding on the secondary structure of the proteins, spectra were recorded using a J-815 circular dichroism spectrometer (JASCO) for a quartz cuvette of 3 mm path length over a wavelength range of 195–300 nm at room temperature. Data were collected every 0.1 nm with a bandwidth of 1 nm at a scanning speed of 50 nm min^{-1} and averaged over three measurements. The proteins (10 $\mu\text{g mL}^{-1}$ or 0.7 μM , in PBS) were incubated with bAgNPs (2 $\mu\text{g mL}^{-1}$, in PBS) for 2 h at room temperature before each measurement. The final spectra were baseline-corrected and the data were measured in mean residue ellipticity (θ) and converted to the standard unit of deg $\text{cm}^2 \text{dmol}^{-1}$ using equation $[\theta] = (\theta \times M_0)/(10\,000 \times C_{\text{soln}} \times L)$, where M_0 denotes the mean residue molecular weight (114 g mol^{-1}), C_{soln} is the protein concentration (g mL^{-1}) and L is the path length through the buffer (cm).

DMD simulations

DMD is a special type of molecular dynamics algorithm with high sampling efficiency, which has been extensively used to model biomolecules. Detailed descriptions for DMD algorithm can be found elsewhere.^{25,31} We used a united atom representation to model the molecular system, explicitly modeling all polar hydrogen and heavy atoms and with implicit solvent. Inter-atomic interactions were modeled by a physical force field adapted from Medusa,^{32,33} which included VDW, solvation, electrostatic and hydrogen bond interactions. The force field parameters for VDW interactions, bond length, angle and dihedrals were taken from CHARMM 19.³⁴ The solvation energy was included using the Lazaridis-Karplus implicit solvent model, EEF1.³⁵ The distance and angular dependant hydrogen bond interaction was modeled using a reaction-like algorithm.³³ We used the Debye-Hückel

approximation to model the screened electrostatic interactions between charged atoms. The Debye length was approximately 1 nm by assuming water relative permittivity of 80, and a monovalent electrolyte concentration of 0.1 M.

We adopted the recently developed AgP molecular mechanics force field²³ to model the AgNP surface. We used the (111) surface with 10 layers of atoms to model the NP surface. The AgP force field included both physical and chemical absorptions, aromatic, and “image” charge interactions. The physical and chemical absorptions as well as aromatic interactions were modeled with Lennard-Jones potentials. The “image” charge interaction was modeled with polarizable dipoles, where a freely-rotatable dipole is attached to each metal atom. We simply attached a charged virtual atom ($-0.3e$) to each metal ($0.3e$) atom with a fixed bond length (1.0 Å) as implemented in the AgP force field. Except the electrostatic interaction, the virtual atoms did not have any other interaction. In order to use the AgP force field in our implicit DMD simulations, we also needed to include the solvation interaction, the solvation energy ΔG_{solv} in the EEF1 model. To determine the optimal ΔG_{solv} , we scanned the value and performed DMD simulations of AgNP binding with various amino acids. We computed the binding energies of various amino acids with an AgNP surface in DMD simulations and compared them with the values obtained from MD simulations using AgP.²³ We estimated the binding energy in DMD simulations as the difference of the averaged potential energy of the bound state with respect to the unbound states. We obtained the best correlation between DMD and MD derived binding energies when $\Delta G_{\text{solv}} = 8.0 \text{ kcal mol}^{-1}$.

The X-ray crystallography structures of lysozyme (PDB code: 1hen) and ALact (PDB code: 1f6s) were used as the reference structures. The dimension of Ag(111) surface was set as $\sim 8 \times 8 \text{ nm}^2$. For the replica exchange simulations, we used 12 replica with temperatures ranging from 275 K to 365 K. For the constant-temperature DMD simulations, 20 independent simulations with different initial conditions of relative distance and orientations were performed in order to reduce any bias of initial configurations and improve sampling statistics. Counter ions (Cl^- , Na^+) were added to render the net charge of the molecular system zero.

Author contributions

DW, VCE, JK, PCK and FD designed and oversaw the project. SS and PCK performed the temperature-controlled DLS experiment, LW performed the TEM experiment, HY and PCK performed the zeta potential experiment, and PC performed the CD experiment. BW and PN performed the computational simulations. PCK and FD wrote the paper and all authors provided inputs to the paper preparation.

Acknowledgements

Ke acknowledges a DVS fellowship from the Office of Chief Executive at CSIRO. This research was sponsored by NSF grant CBET-1232724 (to Ke and Ding), NIH grant R15ES022766-01A1

and Clemson startup funds (to Ding) and funding to the Nanosafety team at CSIRO. The authors thank the Australian Biotech Growth Partnership Theme for supporting the infrastructure needed to complete the experiments.

References

- 1 A. D. Maynard, R. J. Aitken, T. Butz, V. Colvin, K. Donaldson, G. Oberdörster, M. A. Philbert, J. Ryan, A. Seaton and V. Stone, *et al.*, Safe Handling of Nanotechnology, *Nature*, 2006, **444**, 267–269.
- 2 P. C. Ke and M. H. Lamm, A Biophysical Perspective of Understanding Nanoparticles at Large, *Phys. Chem. Chem. Phys.*, 2011, **13**, 7273–7283.
- 3 A. E. Nel, L. Mädler, D. Velegol, T. Xia, E. M. V. Hoek, P. Somasundaran, F. Klaessig, V. Castranova and M. Thompson, Understanding Biophysicochemical Interactions at the Nano-bio Interface, *Nat. Mater.*, 2009, **8**, 543–557.
- 4 I. Lynch and K. A. Dawson, Protein-Nanoparticle Interactions, *Nano Today*, 2008, **3**, 40–47.
- 5 T. Cedervall, I. Lynch, S. Lindman, T. Berggård, E. Thulin, H. Nilsson, K. A. Dawson and S. Linse, Understanding the Nanoparticle-protein Corona Using Methods to Quantify Exchange Rates and Affinities of Proteins for Nanoparticles, *Proc. Natl. Acad. Sci. U. S. A.*, 2007, **104**, 2050–2055.
- 6 M. Lundqvist, J. Stigler, G. Elia, I. Lynch, T. Cedervall and K. A. Dawson, Nanoparticle Size and Surface Properties Determine the Protein Corona with Possible Implications for Biological Impacts, *Proc. Natl. Acad. Sci. U. S. A.*, 2008, **105**, 14265–14270.
- 7 E. Hellstrand, I. Lynch, A. Andersson, T. Drakenberg, B. Dahlbäck, K. A. Dawson, S. Linse and T. Cedervall, Complete High-Density Lipoproteins in Nanoparticle Corona, *FEBS J.*, 2009, **276**, 3372–3381.
- 8 A. Salvati, A. S. Pitek, M. P. Monopoli, K. Prapainop, F. B. Bombelli, D. R. Hristov, P. M. Kelly, C. Åberg, E. Mahon and K. A. Dawson, Transferrin-Functionalized Nanoparticles Lose Their Targeting Capabilities When a Biomolecule Corona Adsorbs on the Surface, *Nat. Nanotechnol.*, 2013, **8**, 137–143.
- 9 Z. J. Deng, M. Liang, M. Monteiro, I. Toth and R. F. Minchin, Nanoparticle-Induced Unfolding of Fibrinogen Promotes Mac-1 Receptor Activation and Inflammation, *Nat. Nanotechnol.*, 2011, **6**, 39–44.
- 10 M. S. Ehrenberg, A. E. Friedman, J. N. Finkelstein, G. Oberdörster and J. L. McGrath, The Influence of Protein Adsorption on Nanoparticle Association with Cultured Endothelial Cells, *Biomaterials*, 2009, **30**, 603–610.
- 11 C. D. Walkey, J. B. Olsen, F. Song, R. Liu, H. Guo, D. W. H. Olsen, Y. Cohen, A. Emili and W. C. W. Chan, Protein Corona Fingerprinting Predicts the Cellular Interaction of Gold and Silver Nanoparticles, *ACS Nano*, 2014, **8**, 2439–2455.
- 12 F. Ding, S. Radic, R. Chen, P. Chen, N. K. Geitner, J. M. Brown and P. C. Ke, Direct Observation of a Single Nanoparticle-ubiquitin Corona Formation, *Nanoscale*, 2013, **5**, 9162–9169.
- 13 W. Shang, J. H. Nuffer, J. S. Dordick and R. W. Siegel, Unfolding of Ribonuclease A on Silica Nanoparticle Surfaces, *Nano Lett.*, 2007, **7**, 1991–1995.
- 14 L. Vroman, A. L. Adams, G. C. Fischer and P. C. Munoz, Interaction of High Molecular Weight Kininogen, Factor XII, and Fibrinogen in Plasma at Interfaces, *Blood*, 1980, **55**, 156–159.
- 15 S. Radic, P. Nedumpully-Govindan, R. Chen, E. Salonen, J. M. Brown, P. C. Ke and F. Ding, Effect of Fullerol Surface Chemistry on Nanoparticle Binding-Induced Protein Misfolding, *Nanoscale*, 2014, **6**, 8340–8349.
- 16 D. F. Moyano, K. Saha, G. Prakash, B. Yan, H. Kong, M. Yazdani and V. M. Rotello, Fabrication of Corona-Free Nanoparticles with Tunable Hydrophobicity, *ACS Nano*, 2014, **8**, 6748–6755.
- 17 M. Mahmoudi, A. M. Abdelmonem, S. Behzadi, J. H. Clement, S. Dutz, M. R. Ejtehadi, R. Hartmann, K. Kantner, U. Linne and P. Maffre, *et al.*, Temperature: The “Ignored” Factor at the NanoBio Interface, *ACS Nano*, 2013, **7**, 6555–6562.
- 18 P. Chen, S. A. Seabrook, V. C. Epa, K. Kurabayashi, A. S. Barnard, D. A. Winkler, J. K. Kirby and P. C. Ke, Contrasting Effects of Nanoparticle Binding on Protein Denaturation, *J. Phys. Chem. C*, 2014, **118**, 22069–22078.
- 19 G. A. Sotiriou and S. E. Pratsinis, Antibacterial Activity of Nanosilver Ions and Particles, *Environ. Sci. Technol.*, 2010, **44**, 5649–5654.
- 20 S. Kittler, C. Greulich, J. Diendorf, M. Köller and M. Epple, Toxicity of Silver Nanoparticles Increases during Storage Because of Slow Dissolution under Release of Silver Ions, *Chem. Mater.*, 2010, **22**, 4548–4554.
- 21 S. Tan, M. Erol, A. Attygalle, H. Du and S. Sukhishvili, Synthesis of Positively Charged Silver Nanoparticles via Photoreduction of AgNO₃ in Branched Polyethyleneimine/HEPES Solutions, *Langmuir*, 2007, **23**, 9836–9843.
- 22 A. Ivask, A. ElBadawy, C. Kaweeteerawat, D. Boren, H. Fischer, Z. Ji, C. H. Chang, R. Liu, T. Tolaymat and D. Telesca, *et al.*, Toxicity Mechanisms in *Escherichia Coli* Vary for Silver Nanoparticles and Differ from Ionic Silver, *ACS Nano*, 2014, **8**, 374–386.
- 23 Z. E. Hughes, L. B. Wright and T. R. Walsh, Biomolecular Adsorption at Aqueous Silver Interfaces: First-Principles Calculations, Polarizable Force-Field Simulations, and Comparisons with Gold, *Langmuir*, 2013, **29**, 13217–13229.
- 24 Y. Okamoto, Generalized-Ensemble Algorithms: Enhanced Sampling Techniques for Monte Carlo and Molecular Dynamics Simulations, *J. Mol. Graphics Modell.*, 2004, **22**, 425–439.
- 25 F. Ding, D. Tsao, H. Nie and N. V. Dokholyan, Ab Initio Folding of Proteins with All-Atom Discrete Molecular Dynamics, *Structure*, 2008, **16**, 1010–1018.
- 26 L. Chen, K. O. Hodgson and S. A. Doniach, Lysozyme Folding Intermediate Revealed by Solution X-Ray Scattering, *J. Mol. Biol.*, 1996, **261**, 658–671.
- 27 T. Kiefhaber, Kinetic Traps in Lysozyme Folding, *Proc. Natl. Acad. Sci. U. S. A.*, 1995, **92**, 9029–9033.

- 28 M. Eleftheriou, R. S. Germain, A. K. Royyuru and R. Zhou, Thermal Denaturing of Mutant Lysozyme with Both the OPLSAA and the CHARMM Force Fields, *J. Am. Chem. Soc.*, 2006, **128**, 13388–13395.
- 29 M. Mahmoudi, I. Lynch, M. R. Ejtehadi, M. P. Monopoli, F. B. Bombelli and S. Laurent, Protein–Nanoparticle Interactions: Opportunities and Challenges, *Chem. Rev.*, 2011, **111**, 5610–5637.
- 30 G. Brancolini, D. B. Kokh, L. Calzolai, R. C. Wade and S. Corni, Docking of Ubiquitin to Gold Nanoparticles, *ACS Nano*, 2012, **6**, 9863–9878.
- 31 D. Shirvanyants, F. Ding, D. Tsao, S. Ramachandran and N. V. Dokholyan, Discrete Molecular Dynamics: An Efficient And Versatile Simulation Method For Fine Protein Characterization, *J. Phys. Chem. B*, 2012, **116**, 8375–8382.
- 32 F. Ding and N. V. Dokholyan, Emergence of Protein Fold Families through Rational Design, *PLoS Comput. Biol.*, 2006, **2**, e85.
- 33 S. Yin, L. Biedermannova, J. Vondrasek and N. V. Dokholyan, MedusaScore: An Accurate Force Field-Based Scoring Function for Virtual Drug Screening, *J. Chem. Inf. Model.*, 2008, **48**, 1656–1662.
- 34 E. Neria, S. Fischer and M. Karplus, Simulation of Activation Free Energies in Molecular Systems, *J. Chem. Phys.*, 1996, **105**, 1902.
- 35 T. Lazaridis and M. Karplus, Effective Energy Functions for Protein Structure Prediction, *Curr. Opin. Struct. Biol.*, 2000, **10**, 139–145.

Supporting Information

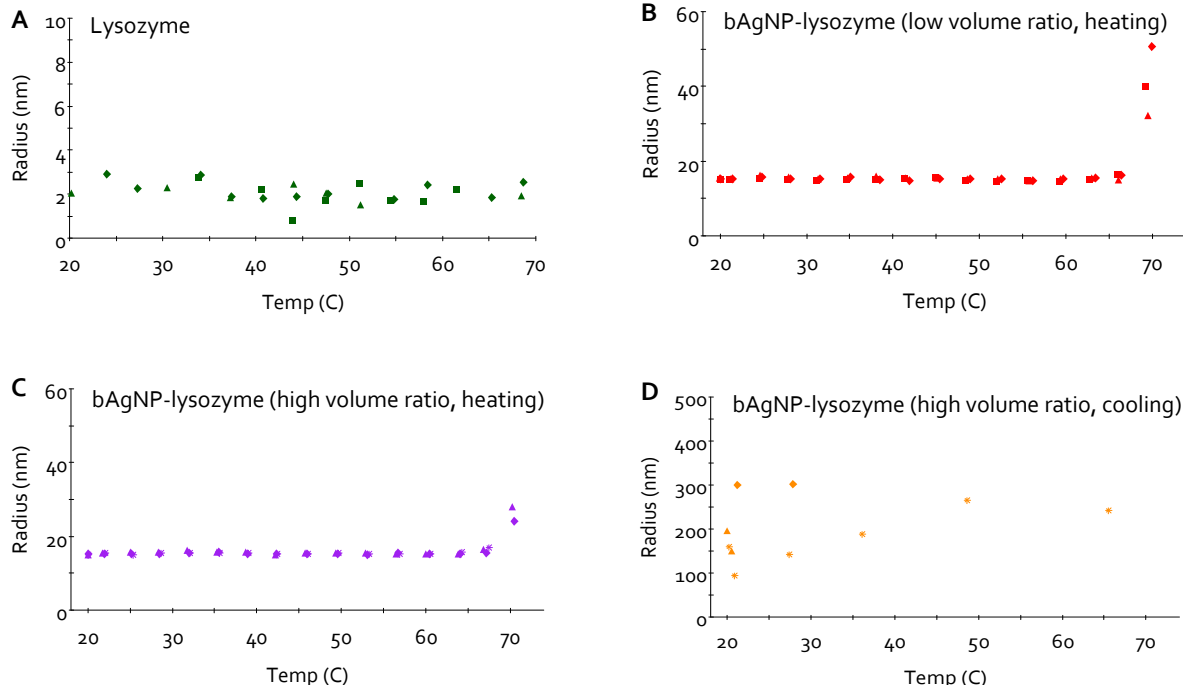


Figure S1. DLS measurement of bAgNP-lysozyme heated from room temperature to 71.4°C and cooled back down to room temperature. (A) Hydrodynamic radius of lysozyme. (B, C) Hydrodynamic radius of bAgNP-lysozyme versus temperature during heating for increasing NP:protein ratios. Lysozyme of 0.9 mg/mL (A-D). bAgNPs of 0.044 mg/mL (B) and 0.088 mg/mL (C, D). (D) Hydrodynamic radius of bAgNP-lysozyme versus temperature during cooling. The diamond, triangles, squares and stars represent data points obtained from different sample wells of the same conditions.

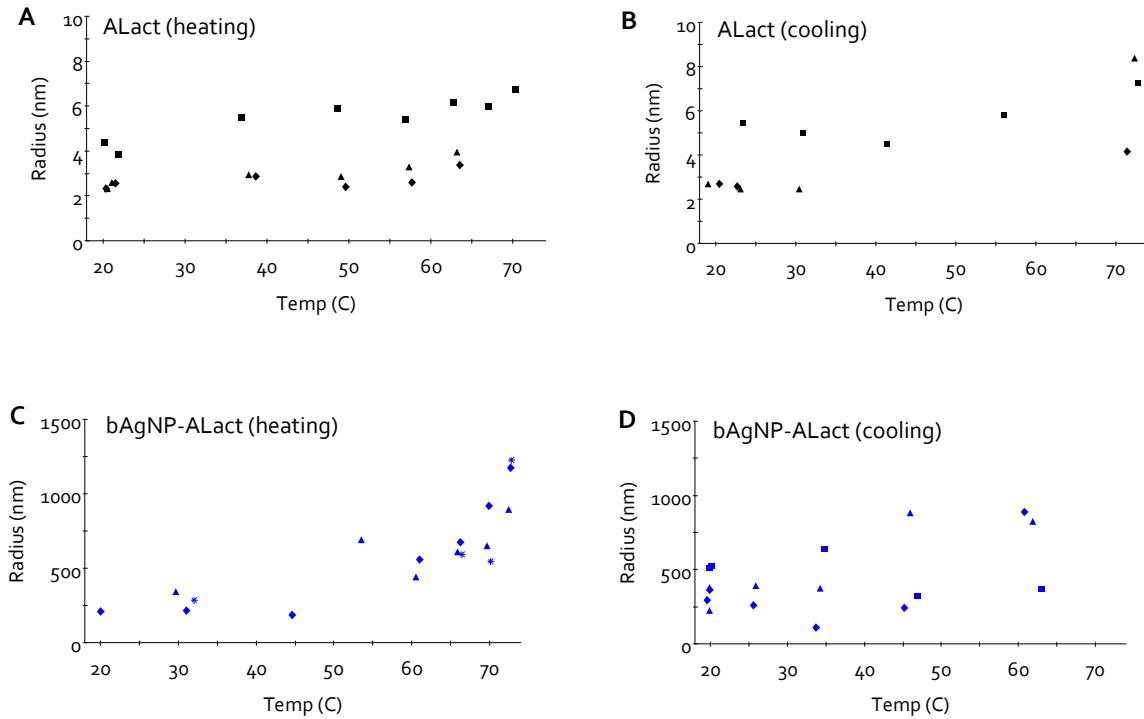


Figure S2. DLS measurement of bAgNP-ALact heated from room temperature to 71.4°C and cooled back down to room temperature. (A, B) Hydrodynamic radius of ALact during heating and cooling. (C, D) Hydrodynamic radius of bAgNP-ALact versus temperature during heating and cooling. ALact: 0.9 mg/mL (A-D). bAgNPs: 0.088 mg/mL (C-D). The diamond, triangles, squares and stars represent data points obtained from different sample wells of the same conditions.

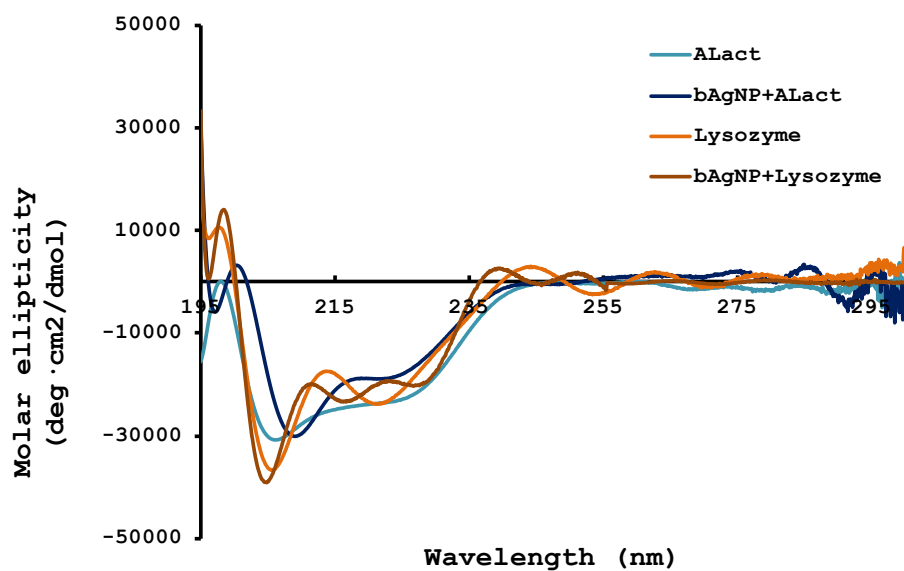


Figure S3. The CD spectra of protein secondary structures in exposure to bAgNPs.

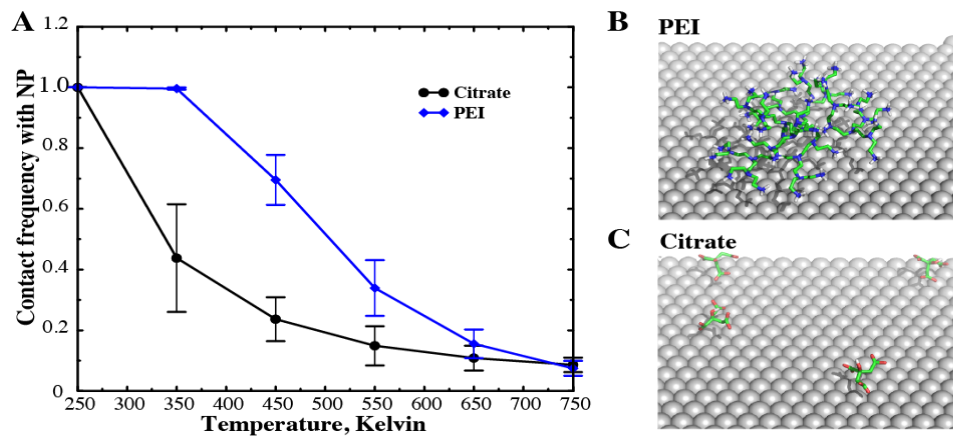


Figure S4. The binding of capping molecules to an AgNP. (A) Two commonly-used capping molecules, citrate and PEI, were studied in DMD simulations. The probability of forming contacts with the NP surface in the simulations was calculated as a function of temperature. PEI displays a stronger binding to NP than citrate because PEI requires a higher temperature to dissociate from the NP surface. The snapshot structures of PEI (B) and citrate (C) bound to NP surface suggest that the strong binding of PEI is due to the electrostatic interactions between the charged amines and their “image” charges.

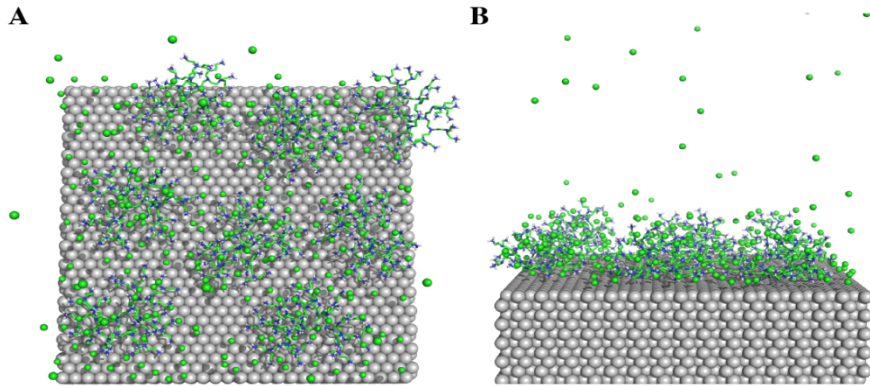


Figure S5. The binding of multiple PEI molecules with an AgNP surface. The counter ions (green spheres) are able to screen the electrostatic repulsion between highly charged PEI molecules (in stick representation), so that multiple PEI molecules can cover the surface of the AgNP to prevent NP-NP aggregation. In our simulations, eight generation-3 PEI dendrimers are able to cover an AgNP surface area of $8.1 \times 8.2 \text{ nm}^2$. Both the top (A) and side (B) views of a PEI-capped NP structure in DMD simulations are shown.

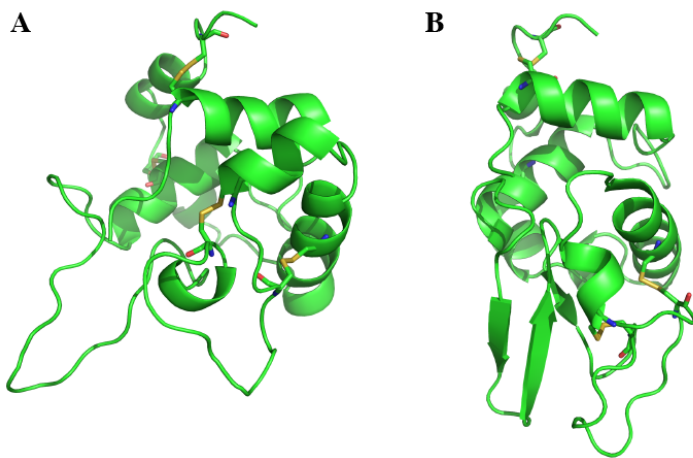


Figure S6. (A) The representative structure of the folding intermediate of lysozyme obtained from DMD simulations. Compared to the native structure (B), the intermediate corresponds to a loss in beta-sheets.